Highly selective production of long-chain aldehydes, ketones or alcohols via syngas at a mild condition

Jing Xu [a,b], Jian Wei [a], Jixin Zhang [a], Ruwei Yao [a,b], Qingjie Ge [a,*], Qingxiang Ma [c], Jian Sun [a,*]

[a] *Dalian National Laboratory for Clean Energy, Dalian Institute of Chemical Physics, Chinese Academy of Sciences, Dalian 116023, China*
[b] *University of Chinese Academy of Sciences, Beijing 100049, China*
[c] *State Key Laboratory of High-efficiency, Utilization of Coal and Green Chemical Engineering, Ningxia University, Yinchuan 750021, China*

ABSTRACT

Tunable synthesis of higher alcohols or formyl compounds (aldehydes and ketones) from syngas is attractive. However, precise control of the coordination between CO dissociative and CO non-dissociative sites, for inactive hydrogenation into aldehyde and ketone are still challenging. Herein, we realized a record-breaking oxygenate selectivity of ~70 wt% in organics at a mild temperature of 170 °C on the K-Fe catalysts, 88% of which is formyl compounds, ranking the highest among the related catalysts. A high selectivity of alcohols of 40.7 wt% is also observed on the Fe catalyst without modification. It is found that K promoter can adjust surface chemical environment (C-rich and H-lean surface) and reaction intermediates, furthermore, can prompt the CO non-dissociative sites from Fe_2C to Fe for alcohol to formyl compound shift. This study provides an alternative strategy to adjust the interaction among active phases and impact on reactant activation to tune the different product distribution.

1. Introduction

Higher oxygenates, typically referred to alcohols, aldehydes and ketones, possessing two or more carbon numbers, have been regarded as valuable chemicals to be directly used for fuels and fuel additives, also as potential intermediates for the synthesis of detergents and surfactants [1–5]. With the aim for high yield via facile and eco-friendly approaches, the direct synthesis of higher oxygenates from syngas is attractive [6–8]. This process is considered to require the coordination of CO dissociative and CO non-dissociative sites, generally the CH_x^* species from CO dissociation undergo insertion reaction with CO^* to form oxygenates [9–12]. However, the difficulties in synergism of the two active sites result in the low oxygenate yield [13–15]. Additionally, the production of aldehydes and ketones need increasingly precise control of hydrogenation activity, making highly selective aldehydes and ketones more challenging.

It is known that Fischer–Tropsch (F–T) synthesis on iron catalyst produces both hydrocarbons and oxygenates. The Fe/Al_2O_3 [16] and Fe_2O_3/Al_2O_3 [17] catalyst have been used for higher alcohol production. Additionally, Durham et al. [18,19] tested Fe/Cu/K catalysts under supercritical-FTS conditions for aldehydes and ketones. The above results confirmed that iron catalysts are promising candidates to produce

oxygenates. However, so far the selectivity of oxygenates is still at a very low level (in all products, alcohol selectivity, nearly 30%; aldehydes and ketones, < 30%). Moreover, iron species in the reaction were unstable and complicated, they could be transformed into each other [20,21], resulting in a lot of controversy over the identification of active sites of oxygenates formation. Some authors regarded Fe as active sites of both CO dissociation and non-dissociation [16], but Fe_2O_3/Al_2O_3 catalyst showed FeO was in charge of higher alcohol formation [17]. In addition, Ando et al. [22] found iron carbides were conducive to hydrocarbon formation, but oxygen species in iron hydroxide (O_{Fe}-OH) may be responsible for methanol. Therefore, it is prerequisite to design a suitable Fe-based catalysts to understand the role of different iron species in higher oxygenate formation and enhance oxygenate selectivity.

Alkali metals are usually introduced into Fe-based catalysts as electronic and structural promoters to enhance the catalytic performance. Specifically, alkali metal as electron donors could influence the activation of reactants and intermediates, moreover, as structural promoters could stabilize the formation of interface sites and active sites. Zhai et al. [23] found Na altered the electronic structure of Fe catalysts, resulting in highly selective production of C_{5+} alkenes. Similarly, our group [24] introduced Na to Fe_3O_4 precipitates to promote alkenes formation. Moreover, K as an electron and structural promoter facilitate to form

---

K_2CO_3-Fe_5C_2 interface sites to synthesize α-alkenes [25]. In addition to above effects of alkali metals on hydrocarbons formation, many researches [26,27] show the addition of alkali metal impact on reactants activation to increase alcohol selectivity. There are few researches on the regulation of iron-based active sites by alkali metals in the production of oxygenates.

Herein, we introduced various alkali metals (Na and K) into the pure iron oxide to regulate product selectivity and clear active sites towards various higher oxygenates. The addition of K into Fe_3O_4 nanoparticles lead to an obviously product shift from alcohols to aldehydes and ketones at a low temperature, the sum selectivity of which reached up to 61.6 wt% with a total oxygenate selectivity of 69.8 wt% (CO_2-free), ranking the highest among all related works. The interaction strength of alkali metals and Fe could tune the fraction of Fe/Fe_2C on spent catalysts, correspondingly, adjust the ratio of formyl compounds and alcohols. This implied that both Fe and Fe_2C are relevant to CO nondissociation, but Fe is more prone to aldehyde and ketone production, instead, Fe_2C for alcohol formation. Molecule-level characterizations and DFT calculations suggest the addition of alkali metals can regulate H_2 and CO activation (C-rich and H-lean surface) and reaction intermediates to promote the highly selective aldehyde and ketone production. This study inspired that making use of alkali metals could adjust the interaction of active phases and impact on reactant activation to tune the product distribution.

2. Experimental

2.1. Catalyst preparation

Pretreatment: commercial Fe_3O_4 (Shanghai Pantian Powder Co., Ltd., 10–20 nm) was pretreated at 350 °C in the air to remove impurities remaining on the surface before using, and marked as pre-Fe.

Wetness impregnation: the aqueous solution of alkali metals ($NaNO_3$, KNO_3 and $CsNO_3$) were impregnated on pre-Fe to obtain different mass fraction of alkali metals. Then the samples were rested and aged at 25 °C for 12 h and dried at 80 °C for 12 h. Finally, they were calcined in air at 500 °C for 3 h to remove the remaining NO_3^-. The obtained catalysts were denoted as nM-Fe, where M and n respectively represent the alkali metal and the amounts of alkali metal loading. For example, 1K-Fe catalyst is that the K loading was 1 wt% (Table S1). Especially, cal-Fe catalyst means the alkali metal loading was 0 wt%, which was prepared only by the calcination of the pre-Fe catalyst.

The α-Fe_2O_3 catalyst was synthesized by precipitation method. Typically, appropriate amount of $Fe(NO_3)_3 \cdot 9\ H_2O$ were dissolved in deionized water, and dropped in $NH_3 \cdot H_2O$ at 60 °C until the PH reached 10. After aging for 1 h, the precipitation was centrifuged and washed until the pH is neutral. In final, it was dried at 80 °C for 12 h and then calcined at 500 °C for 3 h.

2.2. Characterizations

The contents of K promoter and Fe on fresh and spent catalysts were detected on an inductively coupled plasma optical emission spectrometer (ICP-OES, PerkinElmer 7300DV).

X-ray diffraction (XRD) patterns were collected on a PANalytical X′pert Pro diffractometer with Cu Kα radiation at 40 kV and 40 mA.

Fourier transform infrared spectra (FT-IR) was obtained on Nicolet iS50.

The Mössbauer spectra (MES) of Fe species on spent catalysts were tested on a Topologic 500 A spectrometer at room temperature, using 57Co (Rh) radioactive source with a constant acceleration mode.

Transmission electron microscopy (TEM) images of spent catalysts were carried out on a TECNAI G2 F20 instrument (acceleration voltage of 200 kV), and the samples were ultrasonic dispersion for testing.

Scanning electron microscope (SEM) images and EDS mapping were performed on a FEI Quanta FEG 250 equipment.

X-ray photoelectron spectroscopy (XPS) were tested on a Thermo ESCALAB 250XI equipment with Al Kα X-ray source ($hv = 1486.6$ eV and a passing energy of 30 eV).

All temperature programmed experiments were carried out on an Autochem II 2920 instrument. In H_2-temperature programmed reduction (H_2-TPR), 40 mg sample was pretreated at 300 °C for 30 min in pure Ar. When the temperature dropped to 50 °C, the 10% H_2/Ar gas (30 ml/min) was conducted, then raised the temperature to 900 °C (10 °C/min). The signal of H_2 in the outlet gas was constantly detected by TCD. In H_2/CO-temperature programmed desorption (H_2/CO-TPD), 100 mg sample was pretreated at 350 °C for 2 h under pure H_2 atmosphere. After cooling down to 50 °C (the CO-TPD process cool down in Ar stream and need one more adsorption process in flow 5% CO/He for 30 min), the He gas was passed in to flush for 30 min and then the samples was heated to 900 °C (10 °C/min) in flow Ar. H_2/CO desorption signal was detected by mass spectrometer. In temperature programmed surface reaction (TPSR), 100 mg sample was pretreated at 350 °C for 2 h under pure H_2 atmosphere. After cooling down to 50 °C in Ar flow, the gas was converted to 5% CO/He for 30 min and then the sample was flushed for 30 min in Ar stream. Subsequently, it was exposed to 5% H_2/Ar and temperature was raised from 50 °C to 900 °C (10 °C/min). Desorption signal of multiple gases were recorded by mass spectrometer. In O_2-TPO experiment, 100 mg spent sample was heated from 50 °C to 800 °C on 5% O_2/Ar stream. The signal of CO_2 was detected by mass spectrometer.

In situ high pressure diffuse reflectance infrared Fourier transform spectroscopy (DRIFTS) was tested on Thermo Scientific Nicolet 6700. The sample was reduced at 350 °C for 2 h in pure H_2 stream of 30 ml/min and then flushed for 30 min in Ar flow. Subsequently, the sample was cooled down to reaction temperature (190 °C) and the feed gas (H_2/CO = 2, 40 ml/min) was switched to increase the reaction pressure to 4.0 Mpa for continuous detection for 1.5 h.

2.3. Density Functional Theory (DFT) calculation

Periodic DFT method based on the plane wave were used for all calculations, which was implemented in the Vienna Ab Initio Simulation Package (VASP) [28,29]. And the projector augmented wave (PAW) method was performed to describe the electron-ion interaction [30,31]. The electron exchange-correlation energies were evaluated in the Perdew-Burke-Ernzerhof functional (PBE) with the generalized gradient approximation (GGA) [32]. The plane wave basis was 500 eV.

The climb image nudged elastic band (CI-NEB) method with Limited-memory Broyden−Fletcher−Goldfarb−Shanno (LBFGS) optimizer [33,34] has been used to search for the transportation path of H^+ and the saddle points. The initial (reactant) and final (product) configurations are obtained after full relaxation. Five images are inserted along the reaction coordinates between reactant and product.

The adsorption energy could be given by $E_{ads} = E_{X/slab} - [E_{slab} + E_X]$. Specifically, $E_{X/slab}$, E_{slab} and E_X respectively represents the total energy of the slab with adsorbates in equilibrium geometry, the bare slab and the free adsorbates in the gas phase. When the E_{ads} was more negative, the adsorption was the stronger. The reaction energy (E_r) and barrier (E_a) are given by $E_a = G_{IS} - G_{FS}$ (T = 300 K), among them, G_{IS} is the Gibbs free energies of the initial state (IS) and G_{FS} is the energies of corresponding final state (FS). Gibbs free energies of different adsorbates were given by $G = H - T \times S$ and $H = E_{DFT} + E_{ZPE} + E_H$. For example, when CO adsorbs on the substrate (denotes as sub_CO), G(sub_CO) could be calculated by the above formulates, where H(sub_CO) and S(sub_CO) were the enthalpy (eV) and entropy (eV K^{-1}) of sub_CO. In addition, E_{DFT}(sub_CO), E_{ZPE}(sub_CO) and E_H(sub_CO) mean the static electron energy (eV), the zero point energy (eV) and the enthalpy contribution (eV) of sub_CO [35].

Fe_2C (101) surface is cleaved from the bulk Fe_2C with a 2 * 2 * 1 supercell model. The crystal structure of Fe_2C is built according to the previous simulation work [36]. The defined lattice parameters were set up according to the experiment as a=b= 2.794 Å, c= 4.36 Å, α = β = 90°,

$\gamma = 120°$.

2.4. Catalytic test

The CO hydrogenation reaction was tested in a fixed-bed reactor. In general, 1.0 g of catalyst with 20–40 meshes was used for reaction. At first, the catalyst was reduced in H_2 stream (30 ml/min) at 350 °C for 8 h. After reduction, the catalyst was cooled down to 190 °C. Then, the system pressure was increased to 4 Mpa with the feed gas (H_2/CO/N_2 =64/32/4) of 40 ml/min and maintained in the reaction. The reaction was carried out under conditions of 190 °C, 4 Mpa, 2400 ml g^{-1} h^{-1}. The

organic products were directly analyzed by Agilent 8890 equipment (on-line) with flame ionization detector (FID) and HP-1 column. Gas products (N_2, CO, CH_4 and CO_2) were detected by Shimadzu, GC-8A with a thermal conductivity detector and an active charcoal column (TDX-01).

The CO conversion was given by the following Eq. (1):

$$CO\ Conversion(\%) = \frac{CO_{in} - CO_{out}}{CO_{in}} \times 100\% \tag{1}$$

where CO_{in} and CO_{out} respectively mean the moles of CO at the inlet and outlet.

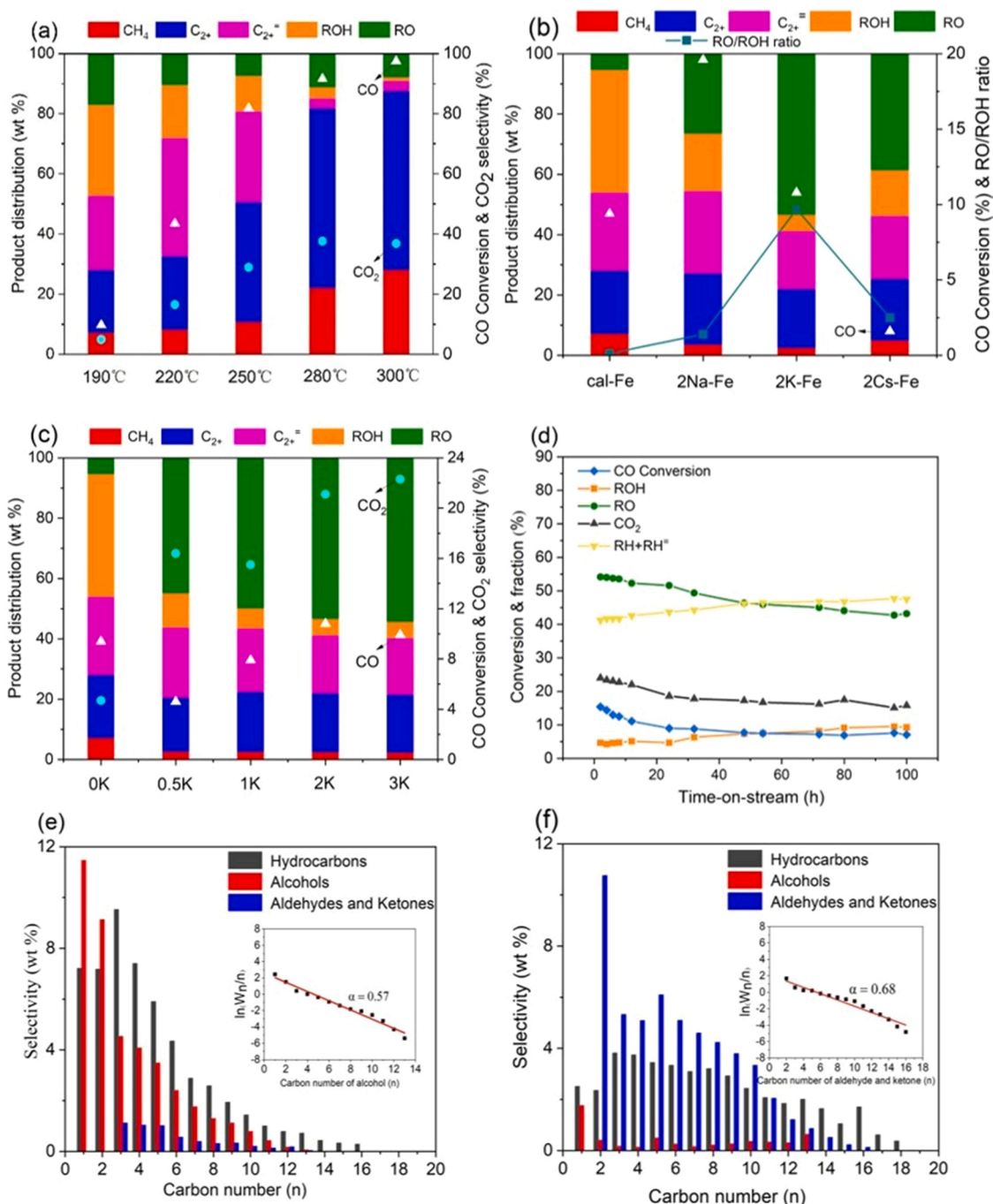The CO_2 selectivity was given by the following Eq. (2):

Fig. 1. Catalytic performance in syngas conversion on various catalysts under the conditions of 190 °C, 4 Mpa, 2400 ml g^{-1} h^{-1}, and H_2/CO= 2. (a) CO conversion and product distribution of pre-Fe catalyst from 190 °C to 300 °C. (b) and (c) CO conversion and product distribution of Fe catalysts with different alkali metals and K contents. (d) Time-on-stream (TOS) experiment over the 2K-Fe catalyst within 100 h. (e) and (f) detailed product distribution over cal-Fe (inset including an ASF plot of alcohol) and 2K-Fe (inset including an ASF plot of aldehyde and ketone).

$$CO_2 \ Selectivity(\%) = \frac{CO_{2out}}{CO_{in} - CO_{out}} \times 100\% \qquad (2)$$

where CO_{2out} denotes the moles of CO_2 at the outlet.

The product (individual hydrocarbon or oxygenates) selectivity S_i was calculated according to the Eq. (3):

$$S_i = \frac{Weight \ of \ i}{Weight \ of \ all \ of \ orangic \ products} \times 100\% \qquad (3)$$

where i means different product i.

3. Results

3.1. Catalytic results

Pretreated Fe_3O_4 support (pre-Fe) was evaluated under conditions of T = 190–300 °C, P = 4 Mpa, H_2/CO = 2, WHSV = 2400 ml $g_{cal}^{-1} h^{-1}$. It was seen from Fig. 1a and Table S2 that CO conversion and CO_2 selectivity dramatically increased when increasing temperature from 190 °C to 300 °C. Additionally, it produced paraffins with high CO conversion at high temperature (>280 °C). To our surprise, Fe_3O_4 support produced significant amounts of long-chain oxygenates including alcohols, aldehydes and ketones at lower temperature, especially below 190 °C. It was seen that up to ~47 wt% oxygenates (ROH/Oxygenate fraction of 87.3%) were obtained for CO conversion of ~10% at 190 °C and $C_{2+}OH$ ratio in ROH distribution reached up to 73.5%, higher than that of 58.3% over α-Fe_2O_3 catalyst (another typical Fe-based catalyst) (Table S3). Additionally, the total ROH selectivity surpassed the most catalysts in syngas conversion to higher alcohols (Table S6). It was summarized that $C_{2+}OH$ generation on Fe_3O_4 support was more favorable than on α-Fe_2O_3 catalyst and its formation was sensitive to reaction temperature (190 °C). The pre-Fe catalyst was further calcined to the cal-Fe catalyst with the same Fe_3O_4 precursor. Similarly, the cal-Fe catalyst also was performed at 190 °C and obtained 46 wt% oxygenates along with a CO conversion of 9.4% (Fig. 1b). Compared with pre-Fe catalyst, it exhibited a tiny performance variation, which indicated on basis of the same Fe_3O_4 precursor, different initial state of iron caused by different calcination temperature had no evident effect on oxygenates generation.

Different alkali metal containing catalysts were prepared and evaluated. As a result, considerable long-chain aldehydes and ketones replaced alcohols as main oxygenates when including alkali metals (Na, K and Cs) into the catalysts (Fig. 1b and Table S4). Specifically, the RO/ROH (RO represents aldehydes and ketones) ratios were 1.4, 9.7 and 2.5 as varying alkali metal from Na, K and Cs. By contrast, catalysts with K showed higher contents of aldehydes and ketones in oxygenates, which exhibited RO selectivity of 53.3 wt% (Aldehyde/RO fraction of 78.7%) with a CO conversion of 10.8%. The results demonstrated moderate basicity could maximize the conversion of alcohols into formyl compounds. Afterwards, different K contents were introduced in the catalysts, it was showed from Fig. 1c and Table S5 that alkanes (especially CH_4) selectivity decreased, CO_2 selectivity increased from 4.7% to 22.3% with the K contents from 0% to 3%. Besides, it was worth noting that CO conversion decreased to 4.6% at 0.5% K, but returned to about 10% when adding 2% K or more. In terms of oxygenates selectivity, a shift from ROH to RO happened when impregnating a small amount of potassium. The highest RO selectivity of 53.3 wt% was obtained at 2% K, the selectivity of aldehydes reached up to 41.9 wt%, which outperformed the most catalysts in CO directly convert to aldehydes (Table S6). Moreover, Time-on-stream test showed the CO conversion remained stable after the first 24 h, but the fraction of alcohols slightly increased during the 100 h on stream (Fig. 1d). In line with Fig. 1c, a surprising shift was seen from product distribution (Fig. 1e,f), which showed the ROH and RO distribution both followed the ASF. Instead, chain growth probability (α) of alcohol was 0.57 on cal-Fe catalyst, and

that of aldehyde and ketone was 0.68 on 2K-Fe catalyst. The product shift and different chain growth probability (α) indicated K may act as a promoter on the active sites responsible for aldehydes and ketones production.

The influences of space-time rate and temperature were investigated on 2K-Fe. The results (see Fig. S1) showed a low temperature and high WHSV were favorable for oxygenate generation, the selectivity further improved to 69.8 wt% (CO_2-free) at 170 °C, 4 Mpa and 5400 ml g_{cal}^{-1} h^{-1} with RO selectivity of 61.6 wt%, which was highest selectivity for RO among the related literature. A lower temperature is believed to facilitate CO insertion and oxygenates production [37], but the alcohol ratio in oxygenates also increases if operating at a too low temperature. By contrast, a high WHSV will shorten the time for aldehyde and ketone hydrogenation, which promote their desorption leading to the large amounts of production for aldehydes and ketones.

3.2. Relationship between iron phases and oxygenation production

To reveal the Fe-based catalysts active sites in oxygenates production, structure and phase of the catalysts were studied. The crystalline structures of the catalysts were shown in XRD patterns. As shown in Fig. 2a, fresh catalysts without K all contained γ-Fe_2O_3, and the α-Fe_2O_3 diffraction peaks only apparently appeared on cal-Fe catalysts. However, the IR spectrum results (Fig. 2b) showed the characteristic peaks [38] corresponding to γ-Fe_2O_3 and α-Fe_2O_3 appeared on both pre-Fe and cal-Fe catalyst, which indicated less α-Fe_2O_3 derived from lower calcined temperature (350 °C) exist and highly dispersed in pre-Fe, in spite of no clear α-Fe_2O_3 diffraction peaks in XRD. Although fresh catalysts presented different γ-Fe_2O_3/α-Fe_2O_3, the spent pre-Fe and cal-Fe catalysts (Fig. S2a) have similar XRD patterns, consisted of iron carbides, Fe_3O_4 and Fe. The phases were further proved by [57]Fe Mössbauer spectroscopy (Figs. S2b and S3). Moreover, the proportions of different Fe species in the two catalysts are also similar, leading to the same alcohol STY and $C_{2+}OH$/ROH fraction at 190 °C (Fig. 1 and Tables S2 and S4). It further illustrates that alcohol formation have no relation to initial state of iron caused by different calcined temperature (including different γ−Fe_2O_3/α-Fe_2O_3), whereas it may depend on the phase balance in CO hydrogenation.

Such viewpoint was proved by totally distinct phases of spent catalysts at different temperatures, whose precursor were all pre-Fe. For the spent pre-Fe catalysts, XRD and Mössbauer spectra (Fig. 2c and d) indicated iron carbides as the main iron species were ascribed to Fe_2C (22.0%) and Fe_5C_2 at low temperature, along with a small quantity of Fe (8.4%). With the reaction temperature increases, the diffraction peaks of Fe_3O_4 gradually strengthened, was believed to be responsible for the water gas shift reaction. As expected, the product selectivity is closely related to the phase states after reaction. The product changed from oxygenates to paraffins and CO_2 as iron species on spent catalysts evidently changed from low- to high- temperature. Correspondence between iron species and product indicated different iron phases were responsible for different products. Specifically, Fe_3O_4 could match with CO_2 production, which is further proved by the product distribution of the raw Fe_3O_4 catalyst (Fig. S4), in line with the literature [39,40]. Besides, the synergy of Fe_5C_2, Fe_2C and Fe contribute the oxygenate formation. Based on our previous work, Fe_5C_2 has already recognized as the CO dissociative sites for CO dissociation and C-C coupling, which is consistent with the literatures in higher alcohol synthesis [7,41]. As a result, Fe_2C and Fe were considered as CO non-dissociation sites for CO insertion, and they combined with Fe_5C_2 to promote oxygenate formation.

3.3. Iron phase transformation in "alcohol to aldehyde and ketone"

The presence or absence of K on the spent catalyst seriously affects the phase of iron (Fig. 3a). With adding K from 0% to 1% or more, the main iron species transformed from Fe_2C (101) and Fe_5C_2 (510) into Fe
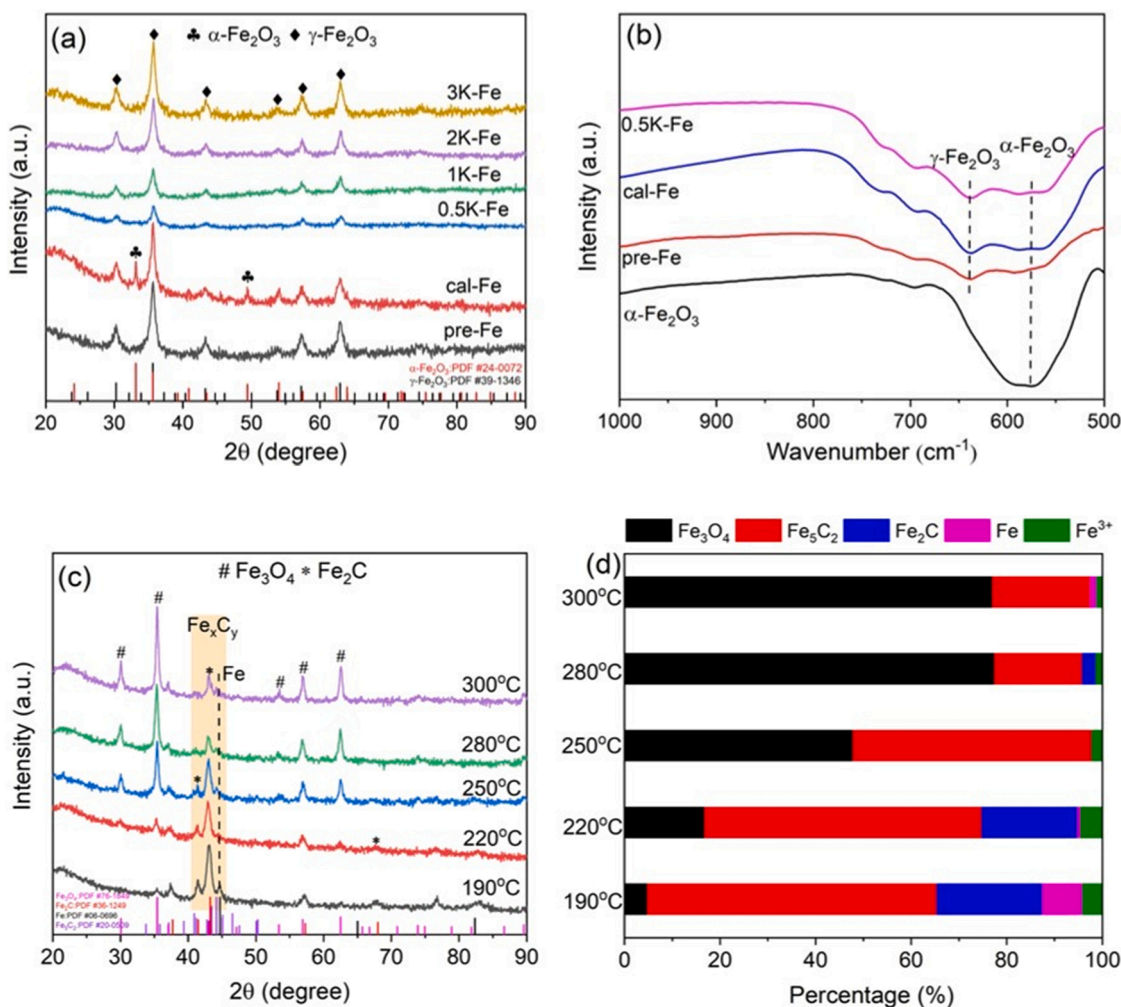
Fig. 2. Phase and structural characterization of Fe-based catalysts with different K contents. (a) XRD pattern of fresh catalysts (pre-Fe: pretreated Fe_3O_4 catalysts). (b) FT-IR spectra of fresh iron oxide with different K contents. (c) XRD patterns and (d) Fe content from Mössbauer spectra of spent pre-Fe catalysts at different reaction temperature.

(110), this is inconsistent with previous reports in the literature [24,25, 42,43]. The reason for the increase of metal iron is found from H_2-TPR and XPS results, which may be associated with the interaction of K-Fe and surface carbon formation. Furthermore, the peak of Fe (110) became sharper and Fe_3O_4 peaks gradually weaken as the rise of K contents, in accordance with the results from ^{57}Fe Mössbauer spectroscopy (Figs. 3b-3d, S5 and Table S7), a great amount of metal iron could not be carbonized, increasing significantly from 7.3% to 41.4%, which corresponds to the change of oxygenates from alcohols to aldehydes and ketones. The iron species transition demonstrated the addition of K changed the carburization behavior of iron, inhibited the formation of iron carbides to promote aldehydes and ketones production. Transmission electron microscopy (TEM) images (Fig. 4a and c) also showed a large amount of exposed Fe (110) on 2K-Fe, but the cal-Fe catalyst only presented iron carbides, including Fe_5C_2 (510) and Fe_2C (101). Additionally, the elemental mapping (Fig. 4b and d) showed all elements were well dispersed on spent cal-Fe catalyst, however, on spent 2K-Fe catalyst, C and O elements were localized dispersed. Iron phase transformation from TEM results further confirmed K enable Fe more stable to synthesize more aldehydes and ketones. And indicated Fe_5C_2-Fe_2C dual-sites synergy on cal-Fe catalyst is in charge of alcohol generation. It is concluded that there may be a strong interaction between K and Fe, which made Fe more stable to become CO insertion active sites to obtain aldehydes and ketones. In contrast, Fe_2C sites were preferable to produce alcohols, especially assisted by a synergistic effect with abundant

neighboring Fe_5C_2, in agreement with the results performed at 190 °C on pre-Fe catalyst (Section 3.2).

To verify the interaction between K and Fe, H_2-TPR was measured (Fig. 5a). In general, the reduction processes of Fe-based catalysts can be divided into two steps, mainly including Fe_2O_3 reduction to Fe_3O_4 at low temperature (300–400 °C) and Fe_3O_4 further transformation into FeO and/or Fe at high temperature (600–800 °C) [44]. It was clearly observed that the reduction peak at low temperature moved to a higher temperature when adding 3% K, which indicated the addition of K inhibited Fe_2O_3 reduction and enhanced the interaction with iron oxide. The interaction between K and Fe were also proved by the Fe $2p_{3/2}$ and K 2p XPS spectra (Figs. 5b-5c and Fig. S6). The XPS results of spent catalysts showed that the Fe $2p_{3/2}$ peak had a significant redshift from 710.6 eV to 710.3 eV when adding K, and along with a shift of K $2p_{3/2}$ peak from 292.8 eV to 293.1 eV. Additionally, the FeC peak also had a slight redshift on 0.5K-Fe catalyst, which indicated the electron transfer from K towards Fe. Moreover, Fe 2p XPS spectra showed that the Fe $2p_{3/2}$ peak intensity gradually decreased and the Fe-C peak disappeared as the rise in the K contents. This result may be relevant to carbon formation on the surface, as shown in the C 1s XPS (Fig. 5d), the peak at 284.8 eV is ascribed to sp^3-hybridized carbon [45], and its peak intensity gradually increased as the increase of K contents. Conversely, the metal carbide peak disappeared, in line with the above result of Fe $2p_{3/2}$ XPS, which further confirmed the addition of K caused carbon formation on the surface, in line with the previous report [46,47]. Moreover,
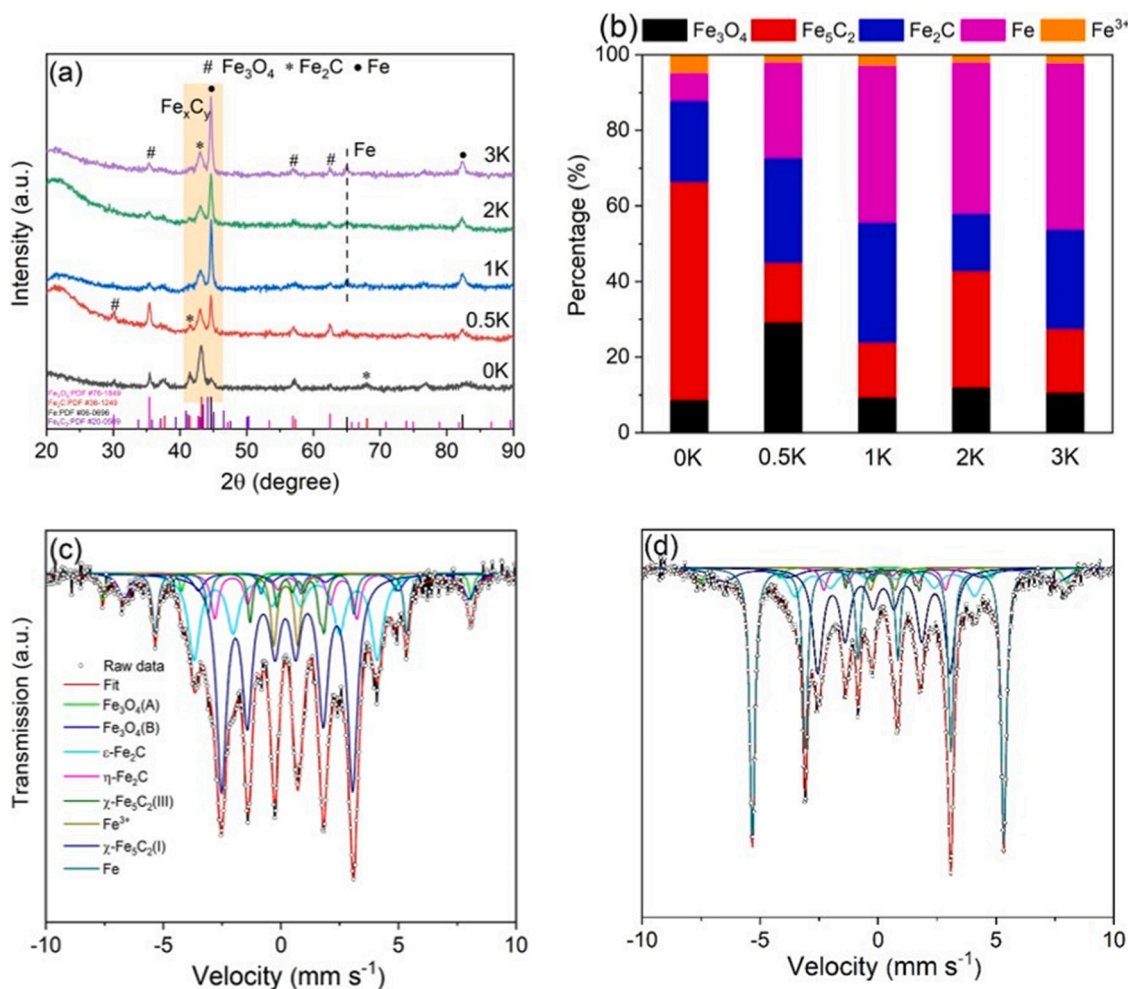
Fig. 3. Phase composition of spent Fe catalysts with different K contents. (a) XRD patterns. (b) Fe content from Mössbauer spectra. ^{57}Fe Mössbauer spectra of (c) spent cal-Fe catalyst and (d) spent 2K-Fe catalyst. Note. All spent catalysts were collected after reacted at 190 °C for 8 h unless otherwise stated.

according the XPS results, the C/Fe ratios on the spent catalysts surface (Table S1) obviously increased from 2.8 to 110.5 as the increase of K contents. Additionally, the O_2-TPO profiles of spent catalysts (Fig. S7) exhibited two peaks of CO_2, corresponding to light coke (100–250 °C) and heavy coke (250–600 °C), respectively [48–50]. The peak area was proportional to the amount of coke. It is obviously observed that peak areas (Table S8) of K-Fe catalysts are larger than pure Fe catalyst, indicating the coke are easier to deposit on K-modified catalysts. These results well proved the existence of stable Fe strongly interacted with K on spent catalysts, as well as the addition of K facilitate carbon formation, as previously reported [51,52]. Carbon formation could compete for C atoms with the formation of carbides, which made it difficult to carbonize Fe. Additionally, some researchers [53,54] reported that deposition of carbonate species might block the active iron phase and restrict the degree of iron carburization.

Moreover, the strength of the interaction between alkali metals and Fe could tune the contents of Fe during the reaction, the point was proved by impregnating different types and contents of alkali metals. When alkali metal from Na to K, and contents from 0.2% to 2%, it was found from the redshift of the Fe 2p peak (Fig. S8) that the alkali metals have a gradually increasing interaction with Fe. More importantly, XRD pattern and Mössbauer spectra of spent catalysts both showed (Fig. 6a and b) that the peaks assigned to Fe became stronger and the contents of Fe were the same order to the strength of the interaction, and increased from 8% to 40%. This result indicated the stronger Fe-alkali interaction could better enhance the stability of Fe and significantly facilitate

metallic iron production of spent catalysts. As mentioned above, more iron metal on spent catalysts was active to CO hydrogenation for aldehydes and ketones, which was well consistent with the results from Fig. 6c. When evaluating the above four samples containing different alkalis and contents (Fig. 6d), a linear increasing relationship between the ratio of Fe/Fe_2C and the fraction of RO/ROH selectivity was established, which further affirmed higher content of iron metal were advantage to forming aldehydes and ketones, instead the amount of Fe_2C determined alcohol yield. Meanwhile, the stability test (Fig. 1) showed the similar correspondence (Supporting information, Fig. S9 and Table S9).

3.4. In situ adsorption-desorption measurements

H_2-TPD and CO-TPD were performed to investigate the influence of K on reaction gas activation. From H_2-TPD (Fig. 7a), two peaks including weak H_2 adsorption (100–250 °C) and strong H_2 adsorption (300–500 °C) could be observed. Focus on our reaction temperature (190 °C), the weak H_2 desorption peak shifted to higher temperature when adding 3% K. More importantly, peak area significantly decreased , especially for 1K- and 2K-Fe catalysts, suggesting that the addition of K weakened the hydrogenation ability of the catalyst. This is similar to TPR results, which can explain the CO conversion reduction in 0.5K-Fe and aldehyde and ketone production in four K-Fe. As for CO-TPD, there were three desorption peaks in Fig. 7b, containing the peak α between 100 and 200 °C (weak CO adsorption), the peak β between
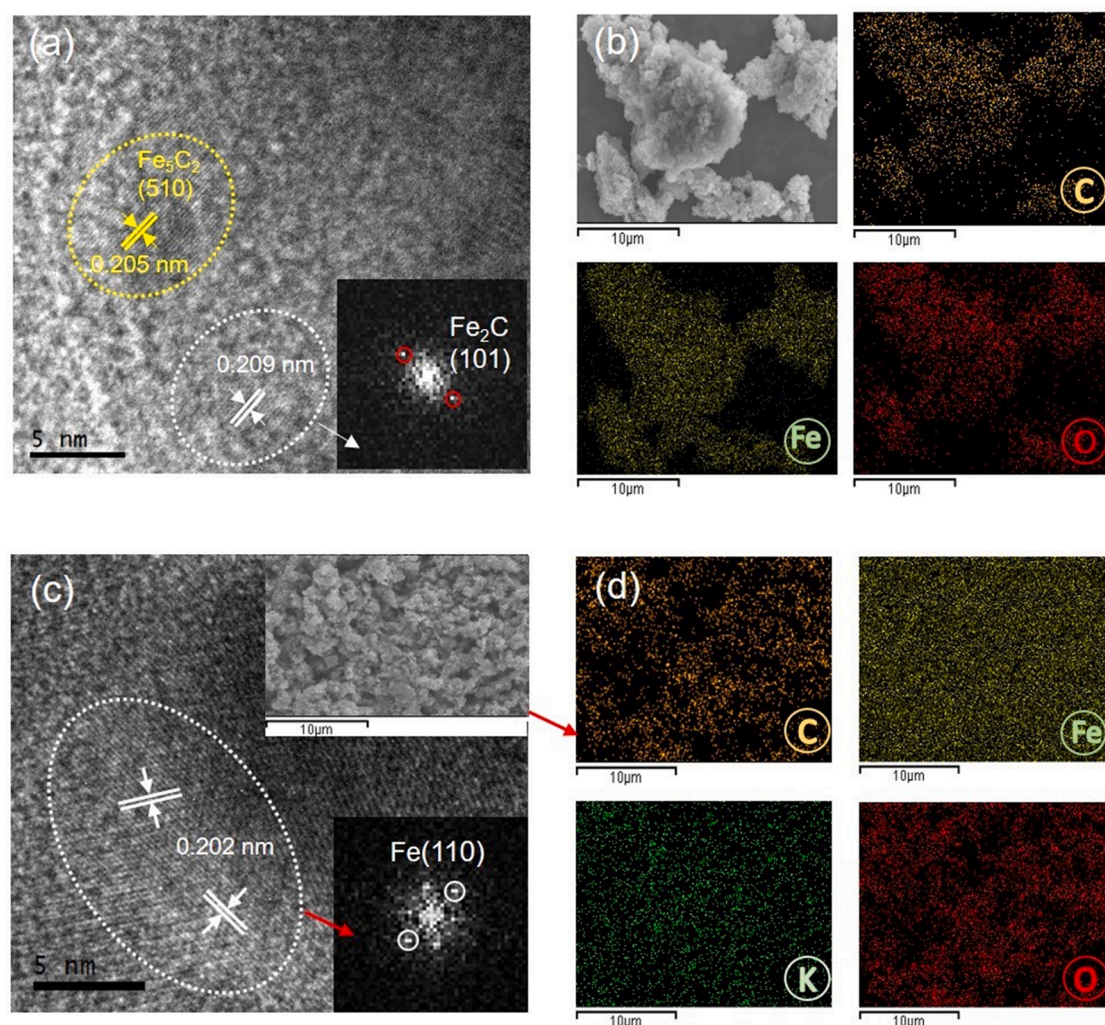
Fig. 4. Transmission electron microscopy (TEM) images, scanning electron microscopy (SEM) images and the corresponding elemental mapping images of different spent catalysts. (a-b) cal-Fe catalysts and (c-d) 2K-Fe catalysts.

350 and 500 °C (medium−strong CO adsorption) and the peak γ above 600 °C (strong CO adsorption). It was evidently seen that weak desorption peaks disappeared and strong desorption peaks moved to higher temperature accompanied with getting greater as increasing K on catalysts. This suggested the addition of K could increase the CO adsorption and enhance the interaction with CO, in agreement with the C1s XPS results. Therefore, a relative C-rich and H-lean surface on Fe particles was induced by the addition of K, this chemical environment prohibited the aldehyde and ketone hydrogenation and accelerated their desorption, which further explain the aldehyde and ketone formation rather than alcohols by adding K.

In order to further verify the above speculation, we introduced the octanal as a co-feedstock with CO and H_2, and performed the octanal-FTS reaction on the catalysts with and without K (Fig. S10 and Table S10). The 73.3% of octanal could convert to octanol on cal-Fe catalysts, 23 times higher than that on 2K-Fe, which was only 3.2% converted. This finding well confirms the fact that the addition of K inhibited aldehyde hydrogenation that leads to the production of large amounts of aldehydes.

To clarify the effect of K on CO dissociative and non-dissociative activation [26,27,35], CO pre-absorbed TPSR tests were performed. CO_2 derived from CO by the water gas shift reaction. Desorption of CH_4 and CO represented CO dissociative and non-dissociative activation in the reaction, respectively. As shown in Fig. 7c, CO desorption temperature ranged from 300 to 900 °C and the areas of the CO desorbed peaks

increased to maximum when the amounts of K increased to 3%, suggesting the presence of K obviously enhances the CO non-dissociation ability, cause more CO molecule insertion to produce oxygenate. This was consistent with the higher total oxygenate selectivity (CO_2-free) on four K-Fe catalysts. As usual, the CH_4 desorption (Fig. 7d) occurred in the temperature from 300 to 700 °C. By observation, the two desorption peaks show no obvious increase or decrease trend with the increase of K content, which demonstrated the catalysts keep CO dissociation ability in the presence or absence of K. In fact, CH_4 selectivity slightly dropped from 7.2% to 2.3%, which is related to hydrogenation suppression ability of K. From insets in Fig. 7c and d, the CO desorption of pre-Fe contained low- and high- temperature desorption peaks, however, only high temperature desorption was observed in the CH_4 desorption, implying CO non-dissociation is more advantageous than dissociation at a low temperature. This could well explain the reason why the pre-Fe catalyst generated oxygenate at low temperature. In addition, the desorption peaks of CO_2 (Fig. S11) represent water gas shift ability. The significantly increase of peak area implied the enhancement of water gas shift ability, which could response the abrupt increase of CO conversion when the K content was above 1%. It was concluded that K could regulate the CO conversion and product selectivity via adjusting CO and H_2 activation in the reaction.

Furthermore, in-situ high pressure DRIFTS measurements were performed to reveal the influence of K on reaction intermediates. As shown in Fig. 8a, b and Table S11, CH_4 and $*CH_x$ from CO dissociation
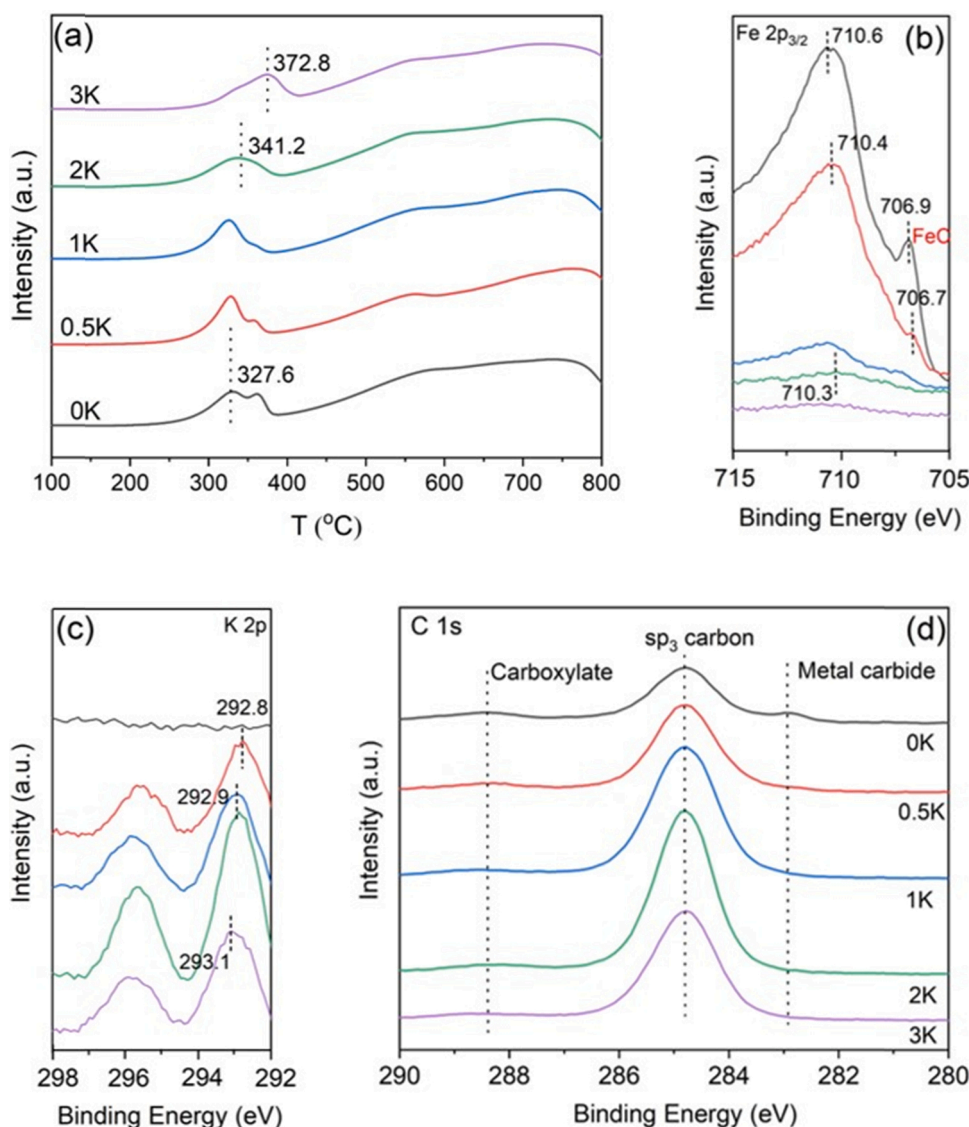
Fig. 5. Interaction between K and Fe of spent Fe catalysts with different K contents. (a) H_2-TPR. XPS spectra (b) Fe $2p_{3/2}$, (c) K 2p and (d) C 1s.

(3015/2964/2933 cm^{-1}) can be observed over cal-Fe and 2K-Fe catalyst, revealing they both have the strong CO dissociative ability, in line with the TPSR results. By contrast, the peak at 1056, 1094 and 3210 cm^{-1} ascribed to $*C_2H_5O$ and $*OH$ from C_2H_5OH were only observed on cal-Fe catalyst. Additionally, as the reaction goes on, the $*C_2H_5O$ and $*OH$ peaks gradually increased, along with the $*CH_3O$ peaks (1073 cm^{-1}) decreased. It indicated the CO insertion into $*CH_3O$ produced C_2H_5OH, resulting in the high selectivity for higher alcohols on cal-Fe catalyst. Similarly, the characteristic peak (1635 cm^{-1}) of $*CH_3CO$ was only found on 2K-Fe catalyst, $*CH_3CO$ hydrogenation could produce CH_3CHO, further implying the addition of potassium facilitate the CH_3CHO formation. Therefore, the addition of K could adjust the intermediates to produce aldehydes and ketones. Besides, as the time goes on under a real reaction pressure, the peaks at 1500–1300 cm^{-1} (see Table S11) assigned to acetate and carbonate were observed on both catalysts, suggesting the possible reaction of CO_2 or adsorbed C_{2+} intermediate species with H_2O produced from the WGS reaction [55].

3.5. Molecule-level mechanism by DFT calculation

DFT calculation were performed to further clarify the CO insertion

mechanism of alcohol and aldehyde formation over cal-Fe and 2K-Fe catalysts in syngas conversion. To simplify the model, Fe_2C (101) and Fe (110) were respectively established to simulate the CO non-dissociative sites in two catalysts. Numerous literatures [56–58] have mentioned that CHO is formed by hydrogen-assisted dissociation from CO, then insertion into CH_2 is more favorable C-C coupling way in ethanol synthesis. Based on the literatures, the more favorable reaction paths were performed on the two active sites. Starting with $*CH_2$ from CO dissociation and $*CO$ from CO non-dissociation, the saturated hydrogenation and C-C coupling could form CH_3CH_2OH, while the unsaturated hydrogenation could produce CH_3CHO. The reaction path for CH_3CH_2OH and CH_3CHO over Fe_2C (101) and Fe (110) were compared in detail. Firstly, both $*CO$ initial activation process for $*CHO$ in ethanol and acetaldehyde synthesis were exothermic process (Fig. 9a, b and Tables S12-S13). However, a heat of 0.653 eV was released for CH_3CHO formation on Fe (110), the energy value of which was 0.275 eV higher than that of CH_3CHO and CH_3CH_2OH formation on Fe_2C (101). This suggested the initial $*CO$ activation was the most thermodynamically favorable on Fe (110) for CH_3CHO formation. Besides, in CH_3CHO synthesis path (Figs. 9a-b, S12 and Table S13), the energy barrier of $*CH_2CHO$ hydrogenation to form a transient state (TS-2) on Fe_2C (101) was 0.93 eV, rather higher than that of 0.61 eV on Fe (110) (Table S13).
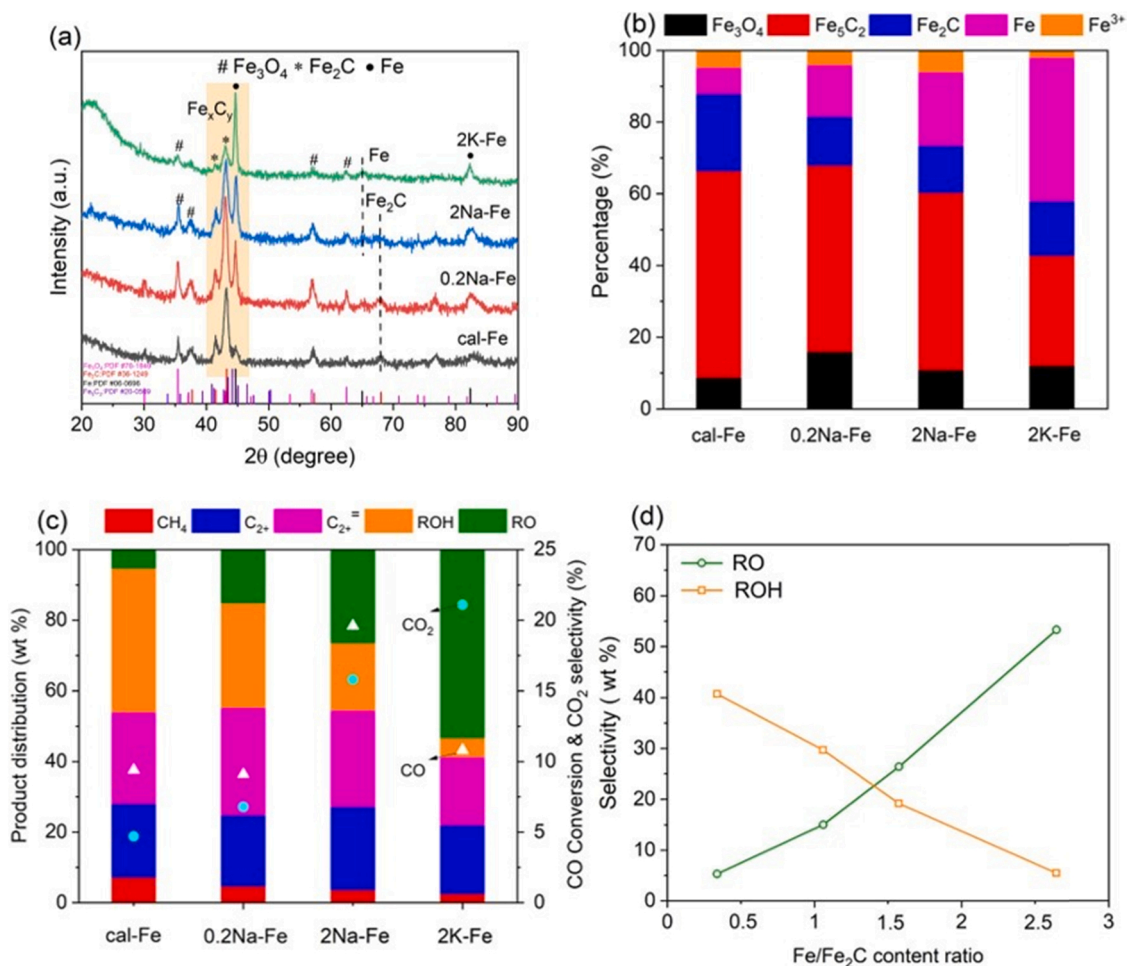
Fig. 6. Structure–performance relationship on Fe catalysts with different alkali metals. (a) XRD patterns of spent catalysts. (b) Fe phase from Mössbauer spectra of spent catalysts. (c) CO conversion and product distribution under the conditions of 190 °C, 4 Mpa, 2400 ml g^{-1} h^{-1}, and H$_2$/CO= 2. (d) correlation of ROH and RO selectivity with the content ratio of Fe/Fe$_2$C on spent Fe catalysts with different alkali metals.

This indicated a more favorable synthesis of aldehyde on Fe (110), in line with previous results on 2K-Fe catalyst. Furthermore, ethanol and acetaldehyde formation on Fe$_2$C (101) were compared (Figs. 9a, S12 and Tables S12–S13). It was evidently found that the corresponding energy barrier of TS-1 transient state formation in ethanol synthesis path was much lower than that of TS-2 transient state in acetaldehyde synthesis path. e.g. 0.47 eV for *CH$_2$CHOH vs 0.93 eV for CH$_3$CHO. This implied that Fe$_2$C active sites were more conducive to alcohol production, which was well consistent with the reaction results on cal-Fe catalyst.

3.6. Structure–Performance Relationship

We further attempt to establish the relationship between oxygenates formation and active sites on our Fe-based catalysts. It is evidently found that RO distribution and ROH distribution both followed ASF distribution. However, the calculated chain growth probability (α), irrespective of formaldehyde, the α value over 2K-Fe is 0.68, in addition, including methanol, α of alcohol is calculated as 0.57. The difference between the two imply that they may have different active sites and follow different reaction routes. However, CO insertion mechanism is widely accepted for oxygenated products formation [4,59–61]. Alcohols were produced by aldehyde and ketone hydrogenation. Therefore, we induce the differences mainly derive from the different active sites.

Based on the former Mössbauer spectra and XRD results, it has been proved that alcohol formation is related to Fe$_2$C species, and different iron phase appears when adding K, specifically, iron metal replaces Fe$_2$C

as the CO non-dissociative active sites to promote aldehyde and ketone production in our reaction. The XPS, H$_2$-TPR and O$_2$-TPO results show the reasons for the stable existence of iron metal are the K-Fe strong interaction and the prohibition of iron carbonization through carbon formation. Moreover, in situ adsorption-desorption experiments demonstrate K can adjust surface chemical environment (C-rich and H-lean surface) and intermediates to promote aldehyde and ketone production. In addition, regardless of whether K is added or not, spent catalysts all contain Fe$_5$C$_2$ species. Based on the previous literatures, it is generally believed that Fe$_5$C$_2$ active sites can be taken as CO dissociative sites for CO dissociation and C-C coupling [7,61]. Therefore, CO non-dissociative sites on our Fe-based catalysts are probably attributed to Fe and Fe$_2$C.

Combined with DFT calculation and all characterizations, we propose a reaction pathway of CO hydrogenation to oxygenates on our Fe-based catalysts, as shown in Fig. 10. The reaction routes of alcohol and formyl compounds synthesis are similar, which mainly involved in two processes, CO dissociation and CO insertion, the former can provide abundant *CH$_x$ species on Fe$_5$C$_2$ reactive sites, they undergo insertion reaction with *CO to form *CH$_x$−*CO coupling, subsequent hydrogenation to obtain alcohol or desorption to obtain aldehyde and ketone. The main difference between the two routes is the CO insertion sites, Fe$_2$C for alcohol synthesis and Fe for aldehyde and ketone synthesis. Additionally, aldehydes and ketones can be easily converted to alcohols by hydrogenation. However, such conversion is severely inhibited by the addition of K. Totally, a highly selective alcohols and formyl compounds
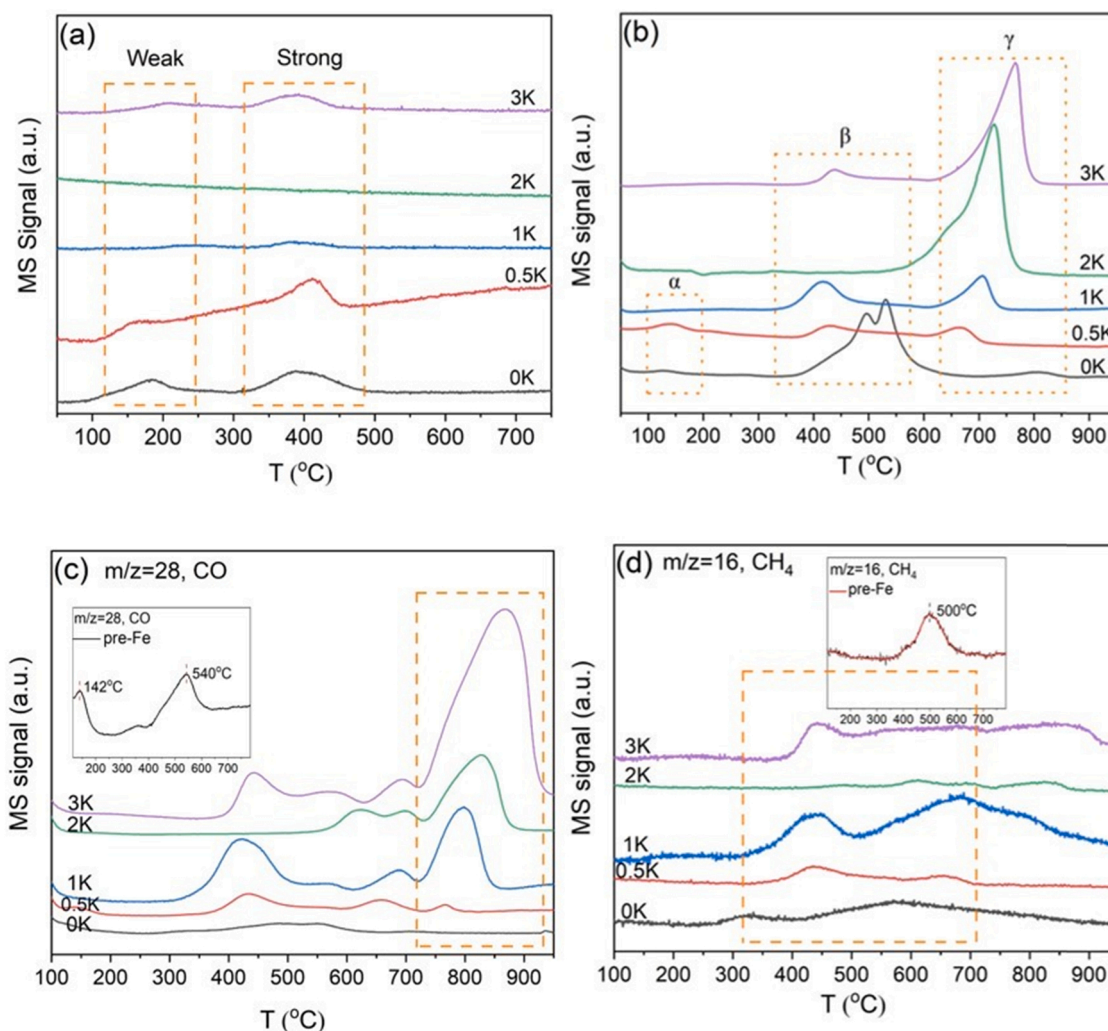
Fig. 7. *In situ* adsorption-desorption measurements on Fe catalysts with different K contents. (a) H_2-TPD. (b) CO-TPD. CO pre-adsorbed TPSR tests: (c) desorption of CO (d) desorption of CH_4.
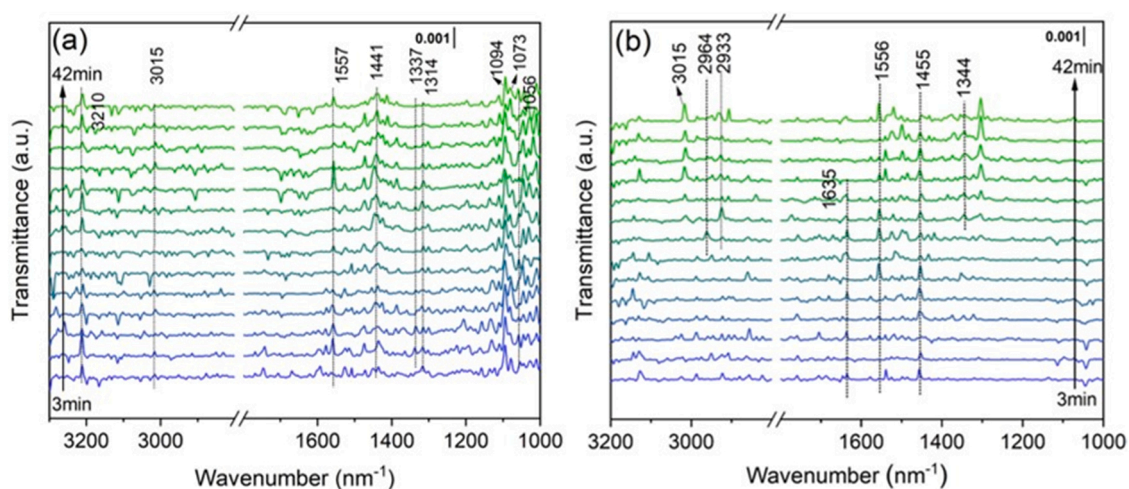

Fig. 8. *In situ* high pressure DRIFTS spectra of (a) cal-Fe catalyst and (b) 2K-Fe catalyst in the $CO+H_2$ atmosphere at 190 °C and 4 Mpa.

are obtained simultaneously.

4. Conclusion

In summary, the production of highly selective alcohol, aldehyde and ketone via syngas could be well tuned over synergistic Fe-K series
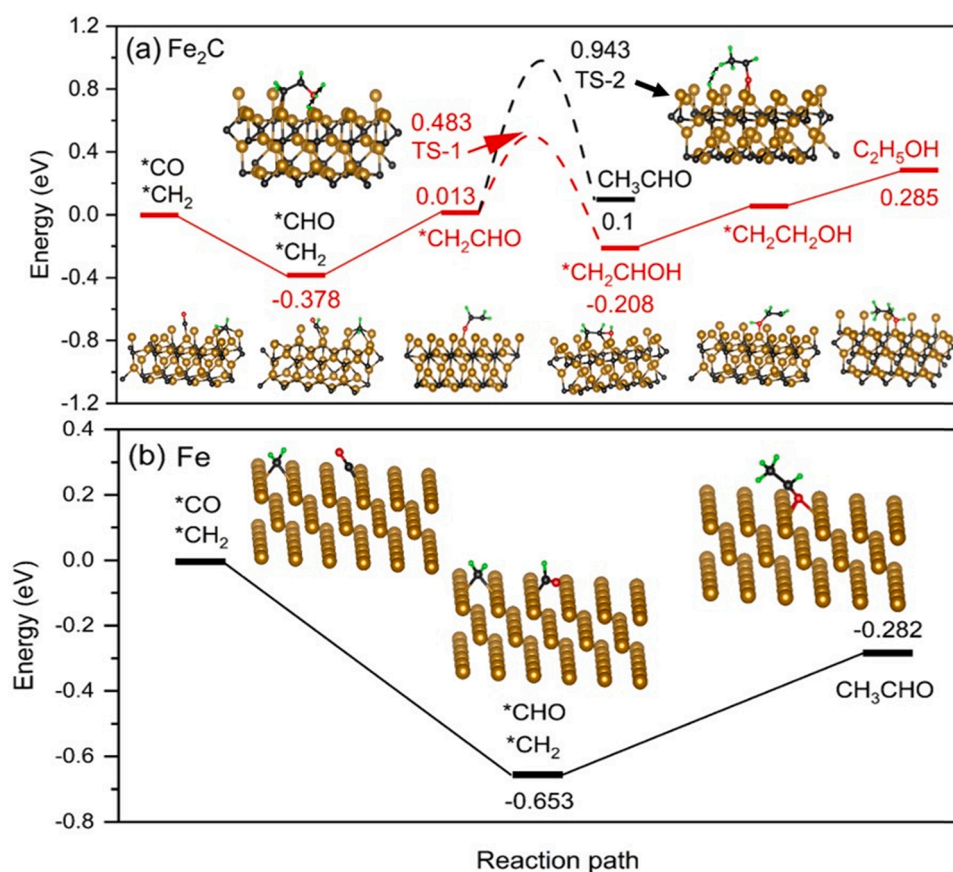
Fig. 9. Reaction path and energy profiles on (a) Fe₂C (101) and (b) Fe (110) by DFT calculations. Fe atom (yellow), C atom (black), H atom (green) and O atom (red) in the profiles.
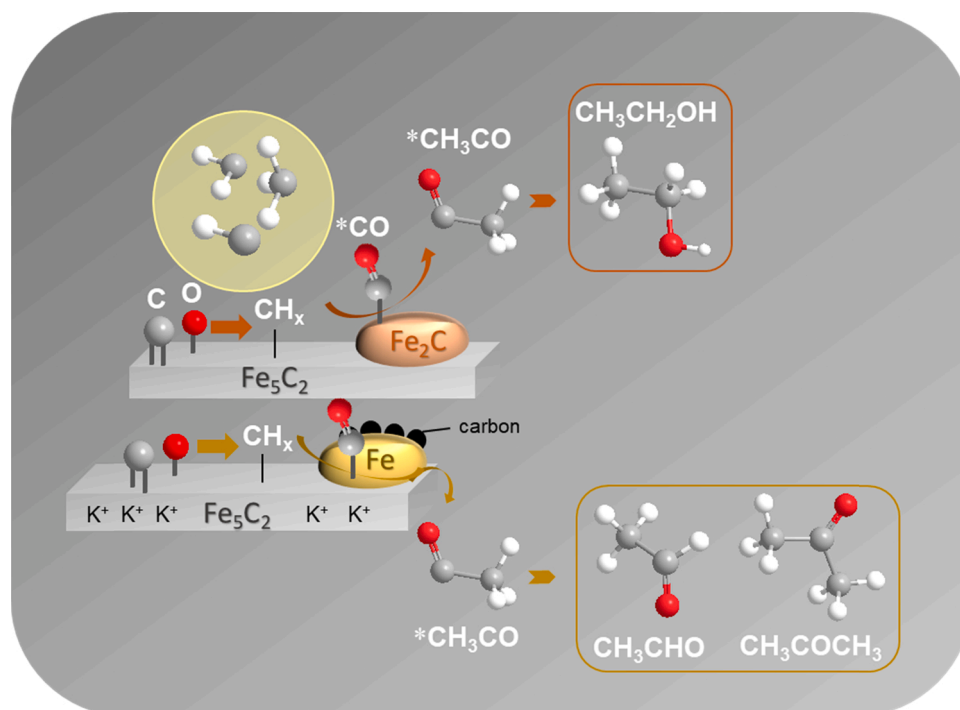

Fig. 10. Illustration for the reaction pathway of oxygenates production over Fe-based catalysts.

catalysts. Pure iron oxides exhibited the outstanding catalytic performance with the sum oxygenates selectivity of 46.0 wt% (CO_2-free), mainly including 40.7 wt% alcohol. When adding 2 wt% potassium, the optimal oxygenate selectivity of 69.8 wt% (CO_2-free) was obtained, the aldehyde and ketone selectivity reached 61.6 wt% on 2K-Fe at a mild condition of 170 °C. The role of potassium is mainly relevant to the CO non-dissociative sites shift from Fe_2C to Fe, which was responsible for aldehyde and ketone formation. The strong interaction between K and Fe species make iron metal stable. Besides, the addition of K enhance carbon formation, which compete for carbon atoms with carbide formation, further inhibit the carbonization of Fe. Additionally, Fe_2C as the main CO non-dissociative sites exists on pure iron oxides for alcohol production. Indeed, this has been confirmed by DFT models. Furthermore, the Fe/Fe_2C ratio could be adjusted by tuning the strength of the interaction between the alkali metal and iron, further leading to change the relative ratio of ROH and RO. On the other hand, K adjust surface chemical environment by changing H_2 and CO activation (C-rich and H-lean surface) and reaction intermediates, resulting in aldehyde and ketone production. This study inspired that making use of alkali metals could adjust the interaction of active phases and impact on reactant activation to tune the different product distribution.

CRediT authorship contribution statement

Jing Xu: Designed experiments, analyzed data and wrote manuscript. **Jian Wei:** discussed and analyzed data. **Jixin Zhang:** discussed and analyzed the experiment. **Ruwei Yao:** discussed the experiment. **Qingjie Ge:** Discussed, revised and supervised the whole project. **Qingxiang Ma:** Support for DFT calculations. **Jian Sun:** Discussed, revised and supervised the whole project.

Declaration of Competing Interest

The authors declare that they have no known competing financial interests or personal relationships that could have appeared to influence the work reported in this paper.

Acknowledgements

Appendix A. Supporting information

Supplementary data associated with this article can be found in the online version at doi:10.1016/j.apcatb.2022.121155.

References

[1] F. Zeng, C. Mebrahtu, X. Xi, L. Liao, J. Ren, J. Xie, H.J. Heeres, R. Palkovits, Catalysts design for higher alcohols synthesis by CO_2 hydrogenation: trends and future perspectives, Appl. Catal. B Environ. 291 (2021), 120073.

[2] H.T. Luk, C. Mondelli, D.C. Ferre, J.A. Stewart, J. Perez-Ramirez, Status and prospects in higher alcohols synthesis from syngas, Chem. Soc. Rev. 46 (2017) 1358–1426.

[3] S. Zhang, Z. Wu, X. Liu, Z. Shao, L. Xia, L. Zhong, H. Wang, Y. Sun, Tuning the interaction between Na and Co_2C to promote selective CO_2 hydrogenation to ethanol, Appl. Catal. B Environ. 293 (2021), 120207.

[4] Y. Xiang, N. Kruse, Tuning the catalytic CO hydrogenation to straight- and long-chain aldehydes/alcohols and olefins/paraffins, Nat. Commun. 7 (2016) 13058.

[5] Y. Lou, F. jiang, W. Zhu, L. Wang, T. Yao, S. Wang, B. Yang, B. Yang, Y. Zhu, X. Liu, CeO_2 supported Pd dimers boosting CO_2 hydrogenation to ethanol, Appl. Catal. B Environ. 291 (2021), 120122.

[6] Y.-P. Pei, J.-X. Liu, J.-H. Zhao, Y.-J. Ding, T. Liu, W.-D. Dong, H.-J. Zhu, H.-Y. Su, L. Yan, J.-L. Li, W.-X. Li, High alcohols synthesis via Fischer–Tropsch reaction at cobalt metal/carbide interface, ACS Catal. 5 (2015) 3620–3624.

[7] Y. Li, W. Gao, M. Peng, J. Zhang, J. Sun, Y. Xu, S. Hong, X. Liu, X. Liu, M. Wei, B. Zhang, D. Ma, Interfacial Fe_5C_2-Cu catalysts toward low-pressure syngas conversion to long-chain alcohols, Nat. Commun. 11 (2020) 61.

[8] X. Xi, F. Zeng, H. Cao, C. Cannilla, T. Bisswanger, S. de Graaf, Y. Pei, F. Frusteri, C. Stampfer, R. Palkovits, H.J. Heeres, Enhanced C_{3+} alcohol synthesis from syngas using $KCoMoS_x$ catalysts: effect of the Co-Mo ratio on catalyst performance, Appl. Catal. B Environ. 272 (2020), 118950.

[9] M. Ao, G.H. Pham, J. Sunarso, M.O. Tade, S. Liu, Active centers of catalysts for higher alcohol synthesis from syngas: a review, ACS Catal. 8 (2018) 7025–7050.

[10] C. Huang, C. Zhu, M. Zhang, J. Chen, K. Fang, Design of efficient ZnO/ZrO_2 modified CuCoAl catalysts for boosting higher alcohol synthesis in syngas conversion, Appl. Catal. B Environ. 300 (2022), 120739.

[11] T. Qin, T. Lin, X. Qi, C. Wang, L. Li, Z. Tang, L. Zhong, Y. Sun, Tuning chemical environment and synergistic relay reaction to promote higher alcohols synthesis via syngas conversion, Appl. Catal. B Environ. 285 (2021), 119840.

[12] W.G. Cui, T.L. Hu, Incorporation of active metal species in crystalline porous materials for highly efficient synergetic catalysis, Small 17 (2021), e2003971.

[13] J. Kang, S. He, W. Zhou, Z. Shen, Y. Li, M. Chen, Q. Zhang, Y. Wang, Single-pass transformation of syngas into ethanol with high selectivity by triple tandem catalysis, Nat. Commun. 11 (2020) 827.

[14] W. Zhou, J. Kang, K. Cheng, S. He, J. Shi, C. Zhou, Q. Zhang, J. Chen, L. Peng, M. Chen, Y. Wang, Direct conversion of syngas into methyl acetate, ethanol, and ethylene by relay catalysis via the intermediate dimethyl ether, Angew. Chem. Int. Ed. 57 (2018) 12012–12016.

[15] W.-G. Cui, Y.-T. Li, H. Zhang, Z.-C. Wei, B.-H. Gao, J.-J. Dai, T.-L. Hu, In situ encapsulated Co/MnO_x nanoparticles inside quasi-MOF-74 for the higher alcohols synthesis from syngas, Appl. Catal. B Environ. 278 (2020), 119262.

[16] M. Pijolat, V. Perrichon, Synthesis of alcohols from CO and H_2 on a Fe/Al_2O_3 catalyst at 8−30 bar pressure, Appl. Catal. 13 (1985) 321−333.

[17] X. Zhang, Z. Li, Q. Guo, H. Zheng, K. Xie, Selective synthesis of mixed alcohols from syngas over catalyst Fe_2O_3/Al_2O_3 in slurry reactor, Fuel Process. Technol. 91 (2010) 379–382.

[18] E. Durham, C. Stewart, D. Roe, R. Xu, S. Zhang, C.B. Roberts, Supercritical Fischer-Tropsch synthesis: heavy aldehyde production and the role of process conditions, Ind. Eng. Chem. Res. 53 (2014) 9695–9702.

[19] E. Durham, S. Zhang, C. Roberts, Diesel-length aldehydes and ketones via supercritical Fischer Tropsch Synthesis on an iron catalyst, Appl. Catal. A Gen. 386 (2010) 65–73.

[20] X. Liu, J. Liu, Y. Yang, Y.-W. Li, X. Wen, Theoretical perspectives on the modulation of carbon on transition-metal catalysts for conversion of carbon-containing resources, ACS Catal. 11 (2021) 2156–2181.

[21] F. Lu, X. Chen, Z. Lei, L. Wen, Y. Zhang, Revealing the activity of different iron carbides for Fischer-Tropsch synthesis, Appl. Catal. B Environ. 281 (2021), 119521.

[22] H. Ando, Y. Matsumura, Y. Souma, Active phase of iron catalyst for alcohol formation in hydrogenation of carbon oxides, Appl. Organomet. Chem. 14 (2000) 831–835.

[23] P. Zhai, C. Xu, R. Gao, X. Liu, M. Li, W. Li, X. Fu, C. Jia, J. Xie, M. Zhao, X. Wang, Y. W. Li, Q. Zhang, X.D. Wen, D. Ma, Highly tunable selectivity for syngas-derived alkenes over zinc and sodium-modulated Fe_5C_2 catalyst, Angew. Chem. Int. Ed. 55 (2016) 9902–9907.

[24] J. Wei, J. Sun, Z. Wen, C. Fang, Q. Ge, H. Xu, New insights into the effect of sodium on Fe_3O_4- based nanocatalysts for CO_2 hydrogenation to light olefins, Catal. Sci. Technol. 6 (2016) 4786–4793.

[25] Y. Han, C. Fang, X. Ji, J. Wei, Q. Ge, J. Sun, Interfacing with carbonaceous potassium promoters boosts catalytic CO_2 hydrogenation of iron, ACS Catal. 10 (2020) 12098–12108.

[26] D. Xu, M. Ding, X. Hong, G. Liu, Mechanistic aspects of the role of K promotion on Cu–Fe-based catalysts for higher alcohol synthesis from CO_2 hydrogenation, ACS Catal. 10 (2020) 14516–14526.

[27] D. Xu, M. Ding, X. Hong, G. Liu, S.C.E. Tsang, Selective C_{2+} alcohol synthesis from direct CO_2 hydrogenation over a Cs-promoted Cu-Fe-Zn catalyst, ACS Catal. 10 (2020) 5250–5260.

[28] A. Gk, B. Jf, Efficiency of ab-initio total energy calculations for metals and semiconductors using a plane-wave basis set, Comput. Mater. Sci. 6 (1996) 15–50.

[29] G. Kresse, J. Furthmüller, Efficient iterative schemes for ab initio total-energy calculations using a plane-wave basis set, Phys. Rev. B Condens. Matter 54 (1996) 11169.

[30] P.E. Blochl, Projector augmented-wave method, Phys. Rev. B Condens. Matter 50 (1994) 17953–17979.

[31] G. Kresse, D. Joubert, From ultrasoft pseudopotentials to the projector augmented-wave method, Phys. Rev. B 59 (1999) 1758–1775.

[32] J. Perdew, K. Burke, M. Ernzerhof, Generalized gradient approximation made simple, Phys. Rev. Lett. 77 (1998) 3865–3868.

[33] G. Henkelman, H. Jónsson, Improved tangent estimate in the nudged elastic band method for finding minimum energy paths and saddle points, J. Chem. Phys. 113 (2000) 9978–9985.

[34] G. Henkelman, B.P. Uberuaga, H. Jónsson, A. Climbing, Image nudged elastic band method for finding saddle points and minimum energy paths, J. Chem. Phys. 113 (2000) 9901–9904.

[35] R. Yao, J. Wei, Q. Ge, J. Xu, Y. Han, Q. Ma, H. Xu, J. Sun, Monometallic iron catalysts with synergistic Na and S for higher alcohols synthesis via CO_2 hydrogenation, Appl. Catal. B Environ. 298 (2021), 120556.

[36] S. Zhao, X.-W. Liu, C.-F. Huo, Y.-W. Li, J. Wang, H. Jiao, Determining surface structure and stability of ε-Fe_2C, χ-Fe_5C_2, θ-Fe_3C and Fe_4C phases under carburization environment from combined DFT and atomistic thermodynamic studies, Catal. Struct. React. 1 (2014) 44–60.

[37] Z. Bao, K. Xiao, X. Qi, X. Wang, L. Zhong, K. Fang, M. Lin, Y. Sun, Higher alcohol synthesis over Cu-Fe composite oxides with high selectivity to $C_{2+}OH$, J. Energy Chem. 22 (2013) 107–113.

[38] Y. Xiong, J. Ye, X. Gu, Q. Chen, Synthesis and assembly of magnetite nanocubes into flux-closure rings, J. Phys. Chem. C 111 (2007) 6998–7003.

[39] Y. Xu, X. Li, J. Gao, J. Wang, G. Ma, X. Wen, Y. Yang, Y. Li, M. Ding, A hydrophobic FeMn@Si catalyst increases olefinsfrom syngas by suppressing C_1 by-products, Science 371 (2021) 610–613.

[40] P. Wang, W. Chen, F.-K. Chiang, A.L. Dugulan, Y. Song, R. Pestman, K. Zhang, J. Yao, B. Feng, P. Miao, W. Xu, E.J.M. Hensen, Synthesis of stable and low-CO_2 selective ε-iron carbide Fischer-Tropsch catalysts, Sci. Adv. 4 (2018), eaau2947.

[41] Y. Lu, B. Cao, F. Yu, J. Liu, Z. Bao, J. Gao, High selectivity higher alcohols synthesis from syngas over three-dimensionally ordered macroporous Cu-Fe catalysts, ChemCatChem 6 (2014) 473–478.

[42] C. Zhang, M. Xu, Z. Yang, M. Zhu, J. Gao, Y.-F. Han, Uncovering the electronic effects of zinc on the structure of Fe_5C_2-ZnO catalysts for CO_2 hydrogenation to linear α-olefins, Appl. Catal. B Environ. 295 (2021), 120287.

[43] J. Wei, Q. Ge, R. Yao, Z. Wen, C. Fang, L. Guo, H. Xu, J. Sun, Directly converting CO_2 into a gasoline fuel, Nat. Commun. 8 (2017) 15174.

[44] Y. Liu, F. Lu, Y. Tang, M. Liu, F.F. Tao, Y. Zhang, Effects of initial crystal structure of Fe_2O_3 and Mn promoter on effective active phase for syngas to light olefins, Appl. Catal. B Environ. 261 (2020), 118219.

[45] M.K. Khan, P. Butolia, H. Jo, M. Irshad, D. Han, K.-W. Nam, J. Kim, Selective conversion of carbon dioxide into liquid hydrocarbons and long-chain α-Olefins over Fe-amorphous AlO_x bifunctional catalysts, ACS Catal. 10 (2020) 10325–10338.

[46] C. Wei, W. Tu, L. Jia, Y. Liu, H. Lian, P. Wang, Z. Zhang, The evolutions of carbon and iron species modified by Na and their tuning effect on the hydrogenation of CO_2 to olefins, Appl. Surf. Sci. 525 (2020), 146622.

[47] S. Yang, H.-J. Chun, S. Lee, S.J. Han, K.-Y. Lee, Y.T. Kim, Comparative study of Olefin production from CO and CO_2 using Na- and K- promoted zinc ferrite, ACS Catal. 10 (2020) 10742–10759.

[48] J. Lu, B. Cao, F. Yu, N. Li, Fe-modified HZSM-5 catalysts for ethanol conversion into light olefins, J. Nat. Gas Chem. 20 (2011) 423–427.

[49] O. Sophiphun, K. Föttinger, S. Loiha, A. Neramittagapong, S. Prayoonpokarach, G. Rupprechter, J. Wittayakun, Properties and catalytic performance in phenol hydroxylation of iron on zeolite beta prepared by different methods, React. Kinet. Mech. Catal. 116 (2015) 549–561.

[50] S.A. Theofanidis, R. Batchu, V.V. Galvita, H. Poelman, G.B. Marin, Carbon gasification from Fe–Ni catalysts after methane dry reforming, Appl. Catal. B Environ. 185 (2016) 42–55.

[51] E. de Smit, F. Cinquini, A.M. Beale, O.V. Safonova, W. van Beek, P. Sautet, B. M. Weckhuysen, Stability and reactivity of ε-χ-θ iron carbide catalyst phases in Fischer-Tropsch synthesis: controlling μ_C, J. Am. Chem. Soc. 132 (2010) 14928–14941.

[52] D. Peña, A. Cognigni, T. Neumayer, W. van Beek, D.S. Jones, M. Quijada, M. Rønning, Identification of carbon species on iron-based catalysts during Fischer-Tropsch synthesis, Appl. Catal. A Gen. 554 (2018) 10–23.

[53] E. de Smit, M.M. van Schooneveld, F. Cinquini, H. Bluhm, P. Sautet, F.M. de Groot, B.M. Weckhuysen, On the surface chemistry of iron oxides in reactive gas atmospheres, Angew. Chem. Int. Ed. 50 (2011) 1584–1588.

[54] D. Peña, L. Jensen, A. Cognigni, R. Myrstad, T. Neumayer, W. vanBeek, M. Rønning, The effect of copper loading on iron carbide formation and surface species in iron-based Fischer-Tropsch synthesis catalysts, ChemCatChem 10 (2018) 1300–1312.

[55] J.W. Magee, R.M. Palomino, M.G. White, Infrared spectroscopy investigation of Fe-promoted Rh catalysts supported on Titania and Ceria for CO hydrogenation, Catal. Lett. 146 (2016) 1771–1779.

[56] B. Ren, X. Dong, Y. Yu, G. Wen, M. Zhang, A density functional theory study on the carbon chain growth of ethanol formation on Cu-Co (111) and (211) surfaces, Appl. Surf. Sci. 412 (2017) 374–384.

[57] Y. Yu, J. Zhang, X. Sun, M. Zhang, Carbon chain growth mechanism of higher alcohols synthesis from syngas on CoCu(100): a combined DFT and kMC study, Surf. Sci. 691 (2020) 121513.

[58] Y.H. Zhao, K. Sun, X. Ma, J. Liu, D. Sun, H.Y. Su, W.X. Li, Carbon chain growth by formyl insertion on rhodium and cobalt catalysts in syngas conversion, Angew. Chem. Int. Ed. 50 (2011) 5335–5338.

[59] T. Lin, X. Qi, X. Wang, L. Xia, C. Wang, F. Yu, H. Wang, S. Li, L. Zhong, Y. Sun, Direct production of higher oxygenates by syngas conversion over a multifunctional catalyst, Angew. Chem. Int. Ed. 58 (2019) 4627–4631.

[60] F. Zeng, X. Xi, H. Cao, Y. Pei, H.J. Heeres, R. Palkovits, Synthesis of mixed alcohols with enhanced C3+ alcohol production by CO hydrogenation over potassium promoted molybdenum sulfide, Appl. Catal. B Environ. 246 (2019) 232–241.

[61] Y. Lu, R. Zhang, B. Cao, B. Ge, F.F. Tao, J. Shan, L. Nguyen, Z. Bao, T. Wu, J. W. Pote, B. Wang, F. Yu, Elucidating the Copper–Hägg iron carbide synergistic interactions for selective CO hydrogenation to higher alcohols, ACS Catal. 7 (2017) 5500–5512.